EUROPEAN ORGANISATION FOR NUCLEAR RESEARCH (CERN)

Submitted to: Phys. Rev. D.

CERN-EP-2022-007
April 25, 2022

Search for the charged-lepton-flavor-violating decay $Z \to e\mu$ in pp collisions at $\sqrt{s} = 13$ TeV with the ATLAS detector

The ATLAS Collaboration

A search for the charged-lepton-flavor-violating process $Z \to e\mu$ is presented, using 139 fb^{-1} of $\sqrt{s} = 13$ TeV pp collision data collected by the ATLAS experiment at the LHC. An excess in the $e\mu$ invariant mass spectrum near the Z boson mass would be a striking signature of new physics. No excess is observed, and an upper limit $\mathcal{B}(Z \to e\mu) < 2.62 \times 10^{-7}$ is placed on the branching fraction at 95% confidence level, which is related to a ratio of the observed $e\mu$ yield to the average of the observed yields of ee and $\mu\mu$ events to significantly reduce systematic uncertainties.

1 Introduction

The observed conservation of charged-lepton flavor is a long-standing mystery. Despite the lack of protection from a fundamental symmetry, no charged-lepton-flavor-violating decays have been observed [1].

Lepton-flavor violation has been observed in the neutrino sector [2, 3], but the rate of charged-lepton-flavor transitions mediated by neutrino-flavor oscillations is expected to be vanishingly small [4], giving, for example[1], $\mathcal{B}(Z \to e\mu) < 4 \times 10^{-60}$. New sources of charged-lepton-flavor violation would indicate physics beyond the Standard Model (BSM), and searches for such violations can be used to constrain BSM theories [5–8].

A search for muon decays into $e^+e^-e^+$ by SINDRUM [9] and a search for $\mu \to e\gamma$ by MEG [10] imply $\mathcal{B}(Z \to e\mu) < 5 \times 10^{-13}$ at 90% confidence level (CL) [11]. However, these interpretations are indirect, and can be evaded in intriguing scenarios, such as anomalous magnetic moments or delicate cancellations [11], which cannot be ruled out. Direct searches for two-body decays into $e\mu$ therefore remain a vital part of the investigation into charged-lepton-flavor violation. Searches at LEP give $\mathcal{B}(Z \to e\mu) < 1.7 \times 10^{-6}$ at 95% CL [12–15] and a previous search at the Large Hadron Collider yielded $\mathcal{B}(Z \to e\mu) < 7.5 \times 10^{-7}$ at 95% CL [16], in 20.3 fb^{-1} of 8 TeV proton collision data collected by the ATLAS experiment. Searches for $Z \to \tau\ell$, where $\ell = e$ or μ, report limits of $\mathcal{B}(Z \to e\tau) < 5.0 \times 10^{-5}$ and $\mathcal{B}(Z \to \mu\tau) < 6.5 \times 10^{-6}$ at 95% CL [17].

This paper presents a search for $Z \to e\mu$ using 139 fb^{-1} of proton collision data collected at $\sqrt{s} = 13$ TeV, in which a boosted decision tree and a veto on b-quark-tagged jets are used to enhance the signal selection.

2 ATLAS detector

The ATLAS detector [18] consists of an inner detector (ID) surrounded by a solenoid that produces a 2 T magnetic field, electromagnetic (EM) and hadronic calorimeters, and a muon spectrometer (MS) immersed in a magnetic field produced by a system of toroidal magnets. The ID measures the trajectories of charged particles over the full azimuthal angle and in the pseudorapidity[2] range of $|\eta| < 2.5$ using silicon pixel, silicon microstrip, and straw-tube transition-radiation tracker detectors. Liquid-argon (LAr) EM sampling calorimeters cover the range $|\eta| < 3.2$ and a scintillator-tile calorimeter provides hadronic calorimetry for $|\eta| < 1.7$. In the endcaps ($|\eta| > 1.5$), LAr is also used for the hadronic calorimeters, matching the outer $|\eta|$ limit of endcap EM calorimeters. The LAr forward calorimeters extend the coverage to $|\eta| < 4.9$ and provide both the EM and hadronic energy measurements. The MS measures the deflection of muons within $|\eta| < 2.7$ using three stations of precision drift tubes, with cathode strip chambers in the innermost station for $|\eta| > 2.0$, and provides separate trigger measurements from dedicated chambers in the region $|\eta| < 2.4$. A trigger system implemented with hardware and software components is used to select interesting events to be recorded for subsequent offline analysis [19]. An extensive software suite [20] is

[1] The electric charges of the lepton pairs throughout the paper are omitted for brevity, but opposite charges are implied except when specified.

[2] ATLAS uses a right-handed coordinate system with its origin at the nominal interaction point (IP) in the center of the detector and the z-axis along the beam pipe. The x-axis points from the IP to the center of the LHC ring, and the y-axis points upward. Cylindrical coordinates (r, ϕ) are used in the transverse plane, ϕ being the azimuthal angle around the beam pipe. The pseudorapidity is defined in terms of the polar angle θ as $\eta = -\ln\tan(\theta/2)$. Transverse momentum and energy are defined relative to the beamline as $p_{\mathrm{T}} = p\sin(\theta)$ and $E_{\mathrm{T}} = E\sin(\theta)$.

used in the reconstruction and analysis of real and simulated data, in detector operations, and in the trigger and data acquisition systems of the experiment.

3 Analysis strategy

The search for flavor-violating decays of the Z boson is performed by examining the invariant mass distribution of opposite-charge $e\mu$ candidates for evidence of a narrow peak consistent with direct Z boson decay. The event selection requires two isolated energetic, oppositely charged leptons of different flavor: $e^{\pm}\mu^{\mp}$. The primary backgrounds consist of decays into τ-lepton pairs ($Z \to \tau\tau \to e\mu\nu\bar{\nu}\nu\bar{\nu}$), decays into muon pairs $Z \to \mu\mu$ where one muon is misidentified as an electron, dileptonic final states from decays of top quark pairs ($t\bar{t} \to e\mu\nu\bar{\nu}b\bar{b}$), and decays of weak boson pairs ($WW \to e\mu\nu\bar{\nu}$). To suppress the contribution from top quark and boson pairs, events are required to have little jet activity and only a small amount of missing transverse momentum. To further reduce the background, a multivariate boosted decision tree (BDT) [21] is trained to distinguish between signal and background events, and the BDT output must exceed a threshold selected to optimize the ratio of expected signal to the square root of the expected background yield. Events from background processes which pass the selection are expected to form a smooth spectrum in the electron–muon invariant mass ($m_{e\mu}$) within the window $70 < m_{e\mu} < 110$ GeV. A binned likelihood fit, in which the signal is unconstrained, is performed. In the absence of a signal, an upper limit on the branching fraction $\mathcal{B}(Z \to e\mu)$ is set, related to a ratio of the observed $e\mu$ yield to the average of the observed yields of ee and $\mu\mu$ events to cancel out common systematic uncertainties.

4 Monte Carlo samples

Samples of simulated collisions generated using Monte Carlo (MC) methods are used to estimate the dominant backgrounds as well as to optimize the event selection. All MC samples were produced using the ATLAS detector simulation [22] based on GEANT44 [23]. Simulated signal $Z \to e\mu$ events were generated at leading order with PYTHIA 8.210 [24] using the A14 set of tuned parameters (tune) [25] and the NNPDF2.3lo parton distribution function (PDF) set [26].

Background events with leptonically decaying W bosons or $Z \to \tau\tau$ production in association with jets were simulated with the SHERPA 2.2.1 [27] generator using next-to-leading-order (NLO) matrix elements for up to two partons, and leading-order (LO) matrix elements for up to four partons, calculated with the COMIX [28] and OPENLOOPS [29–31] libraries. They were matched with the SHERPA parton shower [32] using the MEPS@NLO prescription [33–36] and the set of tuned parameters developed by the SHERPA authors. The NNPDF3.0nnlo set of PDFs [37] was used and the samples were normalized to a cross-section prediction at next-to-next-to-leading order (NNLO) in QCD [38].

Background events with $Z \to \mu\mu$ or $Z \to ee$ in association with jets were modeled with the POWHEG BOX v1 MC generator [39–42] at NLO in the hard-scattering processes of Z boson production. It was interfaced to PYTHIA 8.186 [43] for the modeling of the parton shower, hadronization, and underlying event, with parameters set according to the AZNLO tune [44]. The CT10nlo PDF set [45] was used for the hard-scattering processes, whereas the CTEQ6L1 PDF set [46] was used for the parton shower. The effect of QED final-state radiation was simulated with PHOTOS++ 3.52 [47, 48]. The EVTGEN 1.2.0 program [49] was used to decay bottom and charm hadrons.

All the Z boson samples, including $Z \to \tau\tau$, $Z \to \mu\mu$, $Z \to ee$ and $Z \to e\mu$ events, were reweighted such that the transverse momentum (p_{T}) of the Z boson matches that observed in $Z \to ee$ and $Z \to \mu\mu$ decays in data [50].

Samples of events with fully leptonic diboson final states and semileptonic diboson final states, where one boson decays leptonically and the other hadronically, were simulated with the Sherpa 2.2.1 or 2.2.2 [27] generator depending on the diboson (VV) process, including off-shell effects and Higgs boson contributions where appropriate. They were generated using matrix elements at NLO for up to one additional parton and at LO accuracy for up to three additional parton emissions. Samples for the loop-induced processes $gg \to VV$ were generated using LO-accurate matrix elements for up to one additional parton emission for both the cases of fully leptonic and semileptonic final states. The matrix element calculations were matched and merged with the Sherpa parton shower based on Catani–Seymour dipole factorization [28, 32] using the MEPS@NLO prescription. The virtual QCD corrections were provided by the OpenLoops library. The NNPDF3.0nnlo set of PDFs was used, along with the dedicated set of tuned parton-shower parameters developed by the Sherpa authors. The cross section for the $WW \to e\mu\nu\bar{\nu}$ processes was normalized to a prediction at NNLO in QCD [51].

The top quark backgrounds, i.e. $t\bar{t}$ and single top production, were modeled with the Powheg Box v2 [39–41, 52] generator at NLO, using the four-flavor scheme and the NNPDF3.0nlo set of PDFs. The events were interfaced with Pythia 8.230 using the A14 tune and the NNPDF2.3lo set of PDFs.

Additional pp collisions from the same bunch crossing are included in each event, according to the distribution observed in data. The simulated events are reconstructed with the same software as the data.

5 Object selection

Events are required to have at least one primary collision vertex that has at least two associated tracks, each with transverse momentum $p_{\mathrm{T}} > 0.5$ GeV. The primary vertex is selected as the one with the largest Σp_{T}^2, where the sum is over all tracks with transverse momentum $p_{\mathrm{T}} > 0.4$ GeV that are associated with the vertex.

Candidate electrons are required to have $p_{\mathrm{T}} > 27$ GeV and pseudorapidity $|\eta| < 1.37$ or $1.52 < |\eta| < 2.47$ to ensure they are contained in the high-granularity region of the EM calorimeter and avoid the transition region between the barrel and endcap calorimeters. Candidates must satisfy the "TightLH" identification requirements [53], which are based on calorimeter shower shape, ID track quality, and the spatial match between the shower and the track, as well as the "Tight" isolation requirement [53]. The track parameters z_0 and θ are the longitudinal impact parameter and the polar angle of the electron candidate at the point of closest approach of the track to the beam, respectively. Electrons are required to have a transverse impact parameter with respect to the measured beam position of magnitude less than 5σ, where σ is its estimated uncertainty, and $|z_0 \sin\theta|$ less than 0.5 mm.

Candidate muons are required to have $p_{\mathrm{T}} > 27$ GeV and $|\eta| < 2.5$. Candidates must also satisfy the "Medium" identification requirements [54], which are based on track quality, as well as the "Tight" isolation requirement [55]. Muons are also required to have a transverse impact parameter with respect to the measured beam position of magnitude less than 3σ, and $|z_0 \sin\theta|$ less than 0.5 mm.

Hadronic jets are reconstructed from topological clusters [56] of energy deposits in the EM and hadronic calorimeters using the anti-k_{t} algorithm [57, 58] with distance parameter $R = 0.4$. The topological

clusters are calibrated at the EM energy scale. The jets are fully calibrated using the EM + jet energy scale scheme [59], and required to have $p_{\mathrm{T}} > 20$ GeV and $|\eta| < 2.5$. To reject jets from other pp collisions (pileup), candidate jets with $p_{\mathrm{T}} < 60$ GeV and $|\eta| < 2.4$ are required to pass the jet vertex tagger [60], a likelihood discriminant combining information from several track-based variables.

Jets containing b-hadrons are tagged if they satisfy the requirements of the highest-efficiency working point (85% for jets in $t\bar{t}$ events containing b-hadrons) of the MV2c10 multivariate tagging algorithm [61], which is based on track impact parameters and secondary vertices that are reconstructed from the tracks with large impact parameter significances.

The missing transverse momentum (with magnitude $E_{\mathrm{T}}^{\mathrm{miss}}$) is calculated as the negative vectorial sum of the p_{T} of all reconstructed and calibrated electrons, muons, tau leptons, photons and jets [62, 63], as well as inner-detector tracks originating from the primary vertex but not associated with any reconstructed objects.

6 Event selection

The dataset used in this search was collected during LHC Run 2 in stable beam conditions and with all detector systems operating normally. For this search, performed in 139 fb^{-1} of pp collisions at $\sqrt{s} = 13$ TeV recorded between 2015 and 2018, the candidate events of interest are required to satisfy either a single-electron trigger [64, 65] or a single-muon trigger [66]. Both triggers had p_{T} thresholds that increased from 20 to 26 GeV during the data-taking period.

Events in the signal region are selected by requiring one electron and one oppositely charged muon with an invariant mass in the window $70 < m_{e\mu} < 110$ GeV. Events in the control region are selected by requiring two opposite-charge electrons (muons) with an invariant mass in the window $70 < m_{ee\ (\mu\mu)} < 110$ GeV, to estimate the expected number of Z bosons. Events with more than two candidate leptons are vetoed, using the "Loose" electron [67] or muon [55] identification criteria. To suppress the top quark background, candidate events are vetoed if they contain a leading jet with $p_{\mathrm{T}} > 60$ GeV, or $E_{\mathrm{T}}^{\mathrm{miss}} > 50$ GeV, or any jets tagged as containing b-hadrons.

A machine-learning strategy is used to find the optimal selection in the three-dimensional space of leading jet p_{T}, $E_{\mathrm{T}}^{\mathrm{miss}}$, and $p_{\mathrm{T}}^{e\mu}$ to further suppress the background and enhance the signal; if no jets are reconstructed, a value of zero is used for the leading jet p_{T}. A gradient BDT is trained on samples of simulated signal and background events in the mass window $85 < m_{e\mu} < 95$ GeV, excluding the $Z \to \mu\mu$ background, where large event weights lead to unstable performance in training. The threshold value for the BDT output is chosen by maximizing the ratio of the expected signal to the square root of the expected background. Distributions of BDT values for simulated signal and background events in the mass window $70 < m_{e\mu} < 110$ GeV are shown in Figure 1 along with the ratio of data to MC background events as a function of BDT value. There is no evidence of overtraining, as performance is consistent between testing and training samples.

An analogous selection, but for same-flavor lepton pairs, is applied to build the control region sample used to calculate a normalization which eliminates many systematic uncertainties. For the ee ($\mu\mu$) control region sample, p_{T}^{ee} ($p_{\mathrm{T}}^{\mu\mu}$) is used as an input to the BDT.

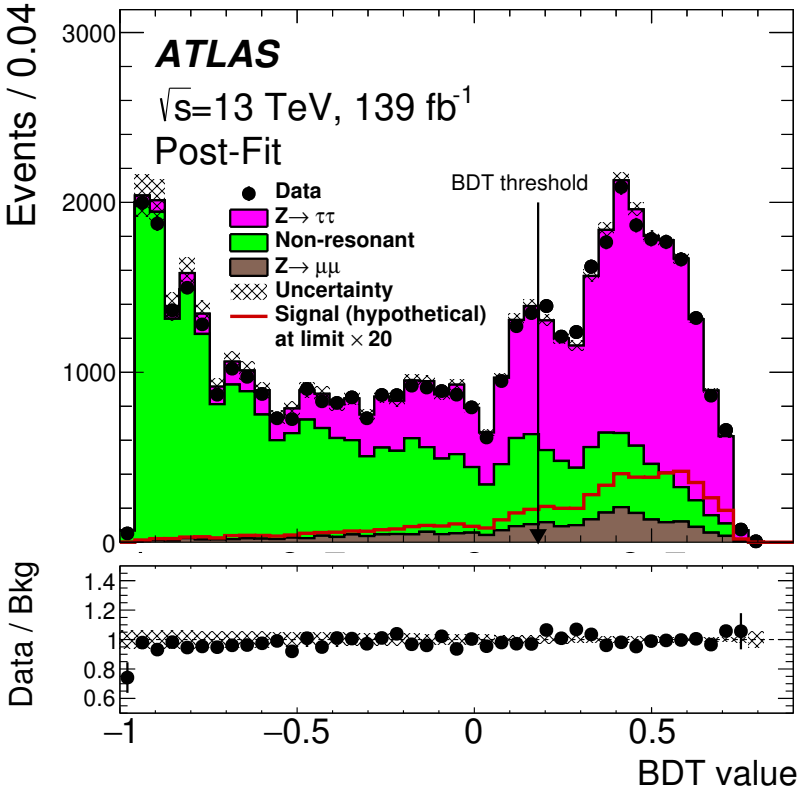

Figure 1: Distributions of BDT values for samples of simulated $Z \to e\mu$ signal and background events (histograms), as well as data (points). The component labeled "non-resonant" includes all SM background processes except $Z \to \tau\tau$ and $Z \to \mu\mu$. The normalizations for the $Z \to \tau\tau$, $Z \to \mu\mu$, and non-resonant background use the best-fit values in Table 1. A hypothetical $Z \to e\mu$ signal, whose branching fraction is set to 20 times the observed upper limit, is shown with a dark red solid line for illustration purposes. The uncertainty band for the MC histogram distribution includes both the systematic and statistical uncertainty. An arrow is added to show the analysis selection requirement for the BDT, corresponding to a value of 0.18.

7 Background estimation

The dominant background in the full mass range considered is due to $Z \to \tau\tau \to e\mu\nu_e\nu_\mu\nu_\tau\nu_\tau$. The subleading background is due to $Z \to \mu\mu$ decays where a muon is misidentified as an electron, due to either muon decay, or radiation of a photon, or an unusually large energy deposit in the EM calorimeter by the muon. Both the $Z \to \tau\tau$ and $Z \to \mu\mu$ contributions are modeled using simulated events.

Additional backgrounds are due to diboson processes, top quark single or pair production, and leptonically decaying W bosons. These backgrounds are modeled using samples of simulated events for studies such as validation of the background estimation method, but these samples are not used in the final likelihood fit. The final background, in which two lepton candidates are misidentified jets, is estimated by extrapolating from samples of data events with leptons of the same electric charge. Assuming that jets are equally likely to be misidentified with either charge, the same-charge contribution is used as an estimate of the opposite-charge contribution, after subtracting previously accounted-for processes, estimated using samples of simulated events, to avoid double-counting. The non-resonant backgrounds, i.e. those other than $Z \to \tau\tau$ and $Z \to \mu\mu$, are the dominant background within the narrower mass range where the signal is

Table 1: Best-fit values of background contributions for the $Z \to \tau\tau$, $Z \to \mu\mu$ and non-resonant backgrounds, from a background-only fit to data corresponding to 139 fb^{-1}, reported for the full mass window $[70, 110]$ GeV, and for a signal-enriched subwindow $[85, 95]$ GeV. The statistical uncertainty, as defined in the text, is shown.

	Best-fit contribution in mass window	
Background	$[70, 110]$ GeV	$[85, 95]$ GeV
$Z \to \tau\tau$	13716 ± 185	951 ± 13
$Z \to \mu\mu$	1557 ± 209	533 ± 72
Non-resonant	4105 ± 259	1075 ± 68

expected. Roughly 80% of this non-resonant background comes from diboson processes and 10% consists of two jets misidentified as lepton candidates. A second-order polynomial function is used to describe the distribution of the non-resonant backgrounds and also to correct for residual differences between the data and the backgrounds estimated from simulation samples, where the normalization and functional parameters float in the fit. The functional form was validated against models of these backgrounds which use samples of simulated events to describe the diboson and top quark contributions and use samples of data and simulated events with leptons of the same electric charge to describe the fake-lepton contributions.

The branching fraction of $Z \to e\mu$ events is estimated using a binned extended maximum-likelihood fit to the $m_{e\mu}$ distribution, where the likelihood is also a function of the number of $Z \to \tau\tau$ events, the number of $Z \to \mu\mu$ events and the number of events due to all non-resonant backgrounds, all of which are free to float in the fit. The distributions in $m_{e\mu}$ for the $Z \to e\mu$ signal and the $Z \to \tau\tau$ and $Z \to \mu\mu$ backgrounds are modeled using histograms based on the samples of simulated events.

8 Results

Distributions of observed events, expected backgrounds after a background-only fit, and a benchmark signal are shown in Figure 2. The spectrum of $m_{e\mu}$ is consistent with the background expectation, with no evidence of an enhancement near the Z boson mass. The best-fit values of the contributions from the various background components are given in Table 1, and are consistent with the numbers from the simulated events and the estimated fake-lepton contributions.

The branching fraction of $Z \to e\mu$, $\mathcal{B}(Z \to e\mu)$, is related to the number of $Z \to e\mu$ decays ($N_{Z\to e\mu}$) divided by the product of the $Z \to e\mu$ signal acceptance and efficiency, $(A \times \varepsilon)_{Z\to e\mu}$, and the number of Z bosons expected in the sample (N_Z^{avg}):

$$N_{Z\to e\mu} = N_Z^{\text{avg}} \times (A \times \varepsilon)_{Z\to e\mu} \times \mathcal{B}(Z \to e\mu) \tag{1}$$

where N_Z^{avg} is the estimate of the number of Z boson events produced, as measured and geometrically averaged from samples of ee and $\mu\mu$ events with invariant mass in the range of $[85, 95]$ GeV, selected with the same requirements as the $e\mu$ sample, other than the same-lepton-flavor requirement, and corrected for background contributions, acceptance times efficiency and the Z leptonic branching ratio. Acceptance and efficiency are measured in samples of simulated events. Comparisons of jet momentum, pseudorapidity and multiplicity in the $Z \to e\mu$ sample, simulated at LO, with the respective quantities in the $Z \to \mu\mu$,

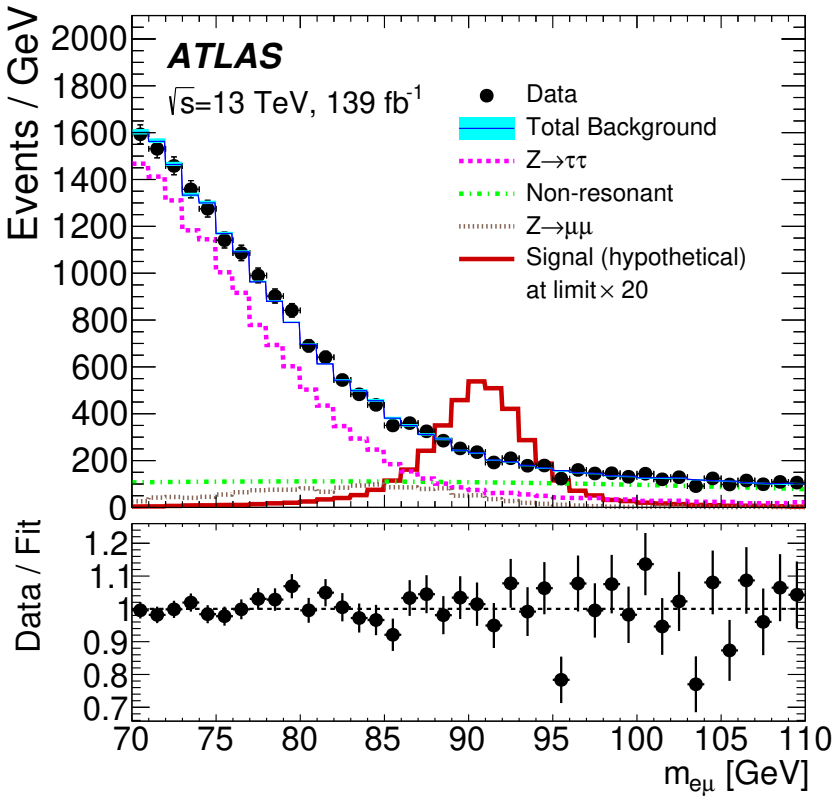

Figure 2: Distribution of the invariant mass $m_{e\mu}$ of the $Z \to e\mu$ candidates, for data (points) and expected backgrounds (lines) after the background-only likelihood fit. The goodness-of-fit, as measured by the χ^2 divided by the number of degrees of freedom is 1.2, with probability 0.24. The final total fit is shown with a blue solid line, the $Z \to \tau\tau$ component with a green dashed line, the $Z \to \mu\mu$ component with a brown dotted line, and the pink dash-dotted curve represents all non-resonant background contributions. The statistical uncertainty is shown with the light blue band. A hypothetical $Z \to e\mu$ signal, its branching fraction scaled to 20 times the observed upper limit, is shown as the dark red solid line for illustration purposes. The lower panel shows the ratio of observed data to expected background yields.

simulated at NLO, show negligible differences after reweighting, and affect the $Z \to e\mu$ branching fraction by less than 0.1%.

The estimate of $\mathcal{B}(Z \to e\mu)$ is extracted using a maximum-likelihood signal-plus-background fit in which $\mathcal{B}(Z \to e\mu)$ is the paramter of interest and which incorporates nuisance parameters for the systematic uncertainties and the parameters of the second-order polynomial function used to model the non-resonant background. The best estimate is $\mathcal{B}(Z \to e\mu) = (0.3 \pm 1.1(\text{stat}) \pm 0.6(\text{syst})) \times 10^{-7}$. The statistical uncertainty is determined by fixing the nuisance parameters to their best-fit values. The systematic uncertainty is determined by subtracting the square of the statistical uncertainty from the square of the total uncertainty. An upper limit on $\mathcal{B}(Z \to e\mu)$ is calculated at 95% CL using a one-sided profile-likelihood test statistic in the asymptotic approximation [68]. The values of $\varepsilon_{Z\to e\mu}$ and N_Z^{avg} are given in Table 2. This method gives a limit which is insensitive to sources of systematic uncertainty which are correlated between the ee, $\mu\mu$ and $e\mu$ final states, such as the jet p_{T} threshold efficiency, modeling of $E_{\text{T}}^{\text{miss}}$ in simulation, and the integrated luminosity.

The dominant remaining systematic uncertainties are due to the statistical uncertainty of the simulated

Table 2: Values of quantities used to calculate $\mathcal{B}(Z \to e\mu)$ via Eq. (1). Quoted uncertainties reflect statistical and systematic contributions.

Quantity	Value
$A \times \varepsilon_{Z\to e\mu}$	$(10.3 \pm 0.3)\%$
N_Z^{avg}	$(7.87 \pm 0.19) \times 10^9$

events used to form histograms of the $Z \to \tau\tau$ and $Z \to \mu\mu$ backgrounds, which are applied independently to each bin, allowing the bin content to vary. The expected upper limit including these uncertainties is 9.5% higher than the limit expected without these uncertainties.

Additional uncertainties include the jet energy scale and resolution uncertainty [59, 69], uncertainties in the efficiency of the jet b-tagging [61], and the pileup reweighting uncertainties [70]. Further sources of systematic uncertainty are the uncertainties in lepton trigger, reconstruction, identification and isolation efficiencies [53, 71]. Electrons have additional uncertainties from energy scale and resolution uncertainties, while muons have uncertainties from momentum resolution, track-to-vertex matching, and sagitta bias correction uncertainties. These additional systematic uncertainties vary the shape of the histograms for the $Z \to e\mu$, $Z \to \tau\tau$ and $Z \to \mu\mu$ processes, and change the signal efficiency. The effects of these additional systematic uncertainties degrade the expected limit by 2.4%. Uncertainties due to higher-order corrections to the simulated $Z \to e\mu$ signal as well as uncertainties due to potential mismodeling of the simulated background processes are found to be negligible.

Any potential bias due to the inability of the chosen polynomial function to accurately describe the background is estimated by fitting the simulated signal-plus-background model to samples of simulated background events. The resulting bias is found to be negligible.

Table 3 shows a summary of the uncertainties and their impact on the expected upper limit of the signal branching fraction $\mathcal{B}(Z \to e\mu)$. The observed (expected) upper limit on the $\mathcal{B}(Z \to e\mu)$ is 2.62 (2.37) $\times 10^{-7}$ at 95% CL, which would correspond to approximately 200 $Z \to e\mu$ reconstructed events. The larger integrated luminosity (139 fb^{-1}) and higher energy ($\sqrt{s}$ = 13 TeV) for this search lower the expected upper limit by a factor of three relative to the previous ATLAS result.

Table 3: Effect of various sources of systematic uncertainty on the expected upper limit on the branching fraction $\mathcal{B}(Z \to e\mu)$, measured by comparing the expected limits obtained with and without a given source of uncertainty. Uncertainties due to the statistical uncertainty of the samples of simulated events used to form the histograms which describe the $Z \to \tau\tau$ and $Z \to \mu\mu$ background processes are treated as systematic uncertainties.

Source of uncertainty	Degradation of $\mathcal{B}^{95\%\text{CL}}(Z \to e\mu)$
Statistical uncertainty in MC samples	9.5%
$Z \to \tau\tau$	4.7%
$Z \to \mu\mu$	6.1%
All other sources	2.4%
Jet energy scale and resolution	1.2%
Pileup	1.2%
Electron energy scale and resolution	0.8%
Lepton efficiency	0.7%
b-tagging	0.6%
Muon resolution and bias correction	0.6%

9 Conclusion

A search for the lepton-flavor-violating process $Z \to e\mu$ is performed in 139 fb^{-1} of $\sqrt{s} = 13$ TeV proton collision data at collected by the ATLAS experiment at the LHC. No localized excess consistent with such a decay is observed in the $m_{e\mu}$ spectrum. An upper limit of $\mathcal{B}(Z \to e\mu) < 2.62 \times 10^{-7}$ is set at 95% CL, a significant improvement on the previous LHC limit, and the most stringent direct result yet reported.

References

[1] S. Mihara, J. Miller, P. Paradisi, and G. Piredda, *Charged Lepton Flavor–Violation Experiments*, Annu. Rev. Nucl. Part. Sci. **63** (2013) 531.

[2] Super-Kamiokande Collaboration, *Solar ^8B and hep Neutrino Measurements from 1258 Days of Super-Kamiokande Data*, Phys. Rev. Lett. **86** (2001) 5651, arXiv: hep-ex/0103032.

[3] SNO Collaboration, *Measurement of the Rate of $\nu_e + d \to p + p + e^-$ Interactions Produced by ^8B Solar Neutrinos at the Sudbury Neutrino Observatory*, Phys. Rev. Lett. **87** (2001) 071301, arXiv: nucl-ex/0106015.

[4] J. I. Illana and T. Riemann, *Charged lepton flavor violation from massive neutrinos in Z decays*, Phys. Rev. D **63** (5 2001) 053004, arXiv: hep-ph/0010193.

[5] J. M. Yang, *Lepton flavor violating Z-boson decays at GigaZ as a probe of supersymmetry*, Sci. China Phys. Mech. Astron. **53** (2010) 1949, arXiv: 1006.2594 [hep-ph].

[6] G.-J. Ding and M.-L. Yan, *Lepton flavor violating $\mu \to e\gamma$ and $\mu - e$ conversion in unparticle physics*, Phys. Rev. D **77** (2008) 014005, arXiv: 0709.3435 [hep-ph].

[7] B. Gripaios, *Composite leptoquarks at the LHC*, JHEP **02** (2010) 045, arXiv: 0910.1789 [hep-ph].

[8] M. Hirsch, A. Vicente, J. Meyer, and W. Porod, *Majoron emission in muon and tau decays revisited*, Phys. Rev. D **79** (2009) 055023, [Erratum: Phys. Rev. D 79, (2009) 079901], arXiv: 0902.0525 [hep-ph].

[9] SINDRUM Collaboration, *Search for the decay* $\mu^+ \to e^+e^+e^-$, Nucl. Phys. B **299** (1988) 1.

[10] MEG Collaboration, *Search for the lepton flavour violating decay* $\mu^+ \to e^+\gamma$ *with the full dataset of the MEG experiment*, Eur. Phys. J. C **76** (2016) 434, arXiv: 1605.05081 [hep-ex].

[11] S. Nussinov, R. D. Peccei, and X. M. Zhang, *Constraints on two-body lepton flavor violating decay processes*, Phys. Rev. D **63** (1 2000) 016003.

[12] OPAL Collaboration, *A Search for lepton flavour violating* Z^0 *decays*, Z. Phys. C **67** (1995) 555.

[13] DELPHI Collaboration, *Search for lepton flavour number violating* Z^0*-decays*, Z. Phys. C **73** (1997) 243.

[14] L3 Collaboration, *Search for lepton flavour violation in Z decays*, Phys. Lett. B **316** (1993) 427.

[15] ALEPH Collaboration, *Searches for new particles in Z decays using the ALEPH detector*, Phys. Rept. **216** (1992) 253.

[16] ATLAS Collaboration, *Search for the lepton flavor violating decay* $Z \to e\mu$ *in pp collisions at* $\sqrt{s} = 8$ *TeV with the ATLAS detector*, Phys. Rev. D **90** (2014) 072010, arXiv: 1408.5774 [hep-ex].

[17] ATLAS Collaboration, *Search for lepton-flavor-violation in Z-boson decays with* τ*-leptons with the ATLAS detector*, Phys. Rev. Lett **127** (1 2021) 271801, arXiv: 2105.12491 [hep-ex].

[18] ATLAS Collaboration, *The ATLAS Experiment at the CERN Large Hadron Collider*, JINST **3** (2008) S08003.

[19] ATLAS Collaboration, *Performance of the ATLAS trigger system in 2015*, Eur. Phys. J. C **77** (2017) 317, arXiv: 1611.09661 [hep-ex].

[20] ATLAS Collaboration, *The ATLAS Collaboration Software and Firmware*, ATL-SOFT-PUB-2021-001, 2021, URL: https://cds.cern.ch/record/2767187.

[21] A. Höcker et al., *TMVA - Toolkit for Multivariate Data Analysis*, (2007), arXiv: physics/0703039.

[22] ATLAS Collaboration, *The ATLAS Simulation Infrastructure*, Eur. Phys. J. C **70** (2010) 823, arXiv: 1005.4568 [physics.ins-det].

[23] GEANT4 Collaboration, *GEANT4–a simulation toolkit*, Nucl. Instrum. Meth. A **506** (2003) 250.

[24] T. Sjöstrand et al., *An introduction to PYTHIA 8.2*, Comput. Phys. Commun. **191** (2015) 159, arXiv: 1410.3012 [hep-ph].

[25] ATLAS Collaboration, *ATLAS Pythia 8 tunes to 7 TeV data*, tech. rep. ATL-PHYS-PUB-2014-021, CERN, 2014, URL: https://cds.cern.ch/record/1966419.

[26] NNPDF Collaboration, *Parton distributions with LHC data*, Nucl. Phys. B **867** (2013) 244, arXiv: 1207.1303 [hep-ph].

[27] E. Bothmann et al., *Event generation with Sherpa 2.2*, SciPost Phys. **7** (2019) 034, arXiv: 1905.09127 [hep-ph].

[28] T. Gleisberg and S. Höche, *Comix, a new matrix element generator*, JHEP **12** (2008) 039, arXiv: 0808.3674 [hep-ph].

[29] F. Buccioni et al., *OpenLoops 2*, Eur. Phys. J. C **79** (2019) 866, arXiv: 1907.13071 [hep-ph].

[30] F. Cascioli, P. Maierhöfer, and S. Pozzorini, *Scattering Amplitudes with Open Loops*, Phys. Rev. Lett. **108** (2012) 111601, arXiv: 1111.5206 [hep-ph].

[31] A. Denner, S. Dittmaier, and L. Hofer, *Collier: A fortran-based complex one-loop library in extended regularizations*, Comput. Phys. Commun. **212** (2017) 220, arXiv: 1604.06792 [hep-ph].

[32] S. Schumann and F. Krauss, *A parton shower algorithm based on Catani-Seymour dipole factorisation*, JHEP **03** (2008) 038, arXiv: 0709.1027 [hep-ph].

[33] S. Höche, F. Krauss, M. Schönherr, and F. Siegert, *A critical appraisal of NLO+PS matching methods*, JHEP **09** (2012) 049, arXiv: 1111.1220 [hep-ph].

[34] S. Höche, F. Krauss, M. Schönherr, and F. Siegert, *QCD matrix elements + parton showers: The NLO case*, JHEP **04** (2013) 027, arXiv: 1207.5030 [hep-ph].

[35] S. Catani, F. Krauss, B. R. Webber, and R. Kuhn, *QCD Matrix Elements + Parton Showers*, JHEP **11** (2001) 063, arXiv: hep-ph/0109231.

[36] S. Höche, F. Krauss, S. Schumann, and F. Siegert, *QCD matrix elements and truncated showers*, JHEP **05** (2009) 053, arXiv: 0903.1219 [hep-ph].

[37] R. D. Ball et al., *Parton distributions for the LHC run II*, JHEP **04** (2015) 040, arXiv: 1410.8849 [hep-ph].

[38] C. Anastasiou, L. J. Dixon, K. Melnikov, and F. Petriello, *High precision QCD at hadron colliders: Electroweak gauge boson rapidity distributions at next-to-next-to leading order*, Phys. Rev. D **69** (2004) 094008, arXiv: hep-ph/0312266.

[39] P. Nason, *A new method for combining NLO QCD with shower Monte Carlo algorithms*, JHEP **11** (2004) 040, arXiv: hep-ph/0409146.

[40] S. Frixione, P. Nason, and C. Oleari, *Matching NLO QCD computations with parton shower simulations: the POWHEG method*, JHEP **11** (2007) 070, arXiv: 0709.2092 [hep-ph].

[41] S. Alioli, P. Nason, C. Oleari, and E. Re, *A general framework for implementing NLO calculations in shower Monte Carlo programs: the POWHEG BOX*, JHEP **06** (2010) 43.

[42] S. Alioli, P. Nason, C. Oleari, and E. Re, *NLO vector-boson production matched with shower in POWHEG*, JHEP **07** (2008) 060, arXiv: 0805.4802 [hep-ph].

[43] T. Sjöstrand, S. Mrenna, and P. Skands, *A brief introduction to PYTHIA 8.1*, Comput. Phys. Commun. **178** (2008) 852, arXiv: 0710.3820 [hep-ph].

[44] ATLAS Collaboration, *Measurement of the Z/γ^* boson transverse momentum distribution in pp collisions at $\sqrt{s} = 7$ TeV with the ATLAS detector*, JHEP **09** (2014) 145, arXiv: 1406.3660 [hep-ex].

[45] H.-L. Lai et al., *New parton distributions for collider physics*, Phys. Rev. D **82** (2010) 074024, arXiv: 1007.2241 [hep-ph].

[46] J. Pumplin et al.,
New Generation of Parton Distributions with Uncertainties from Global QCD Analysis,
JHEP **07** (2002) 012, arXiv: hep-ph/0201195.

[47] P. Golonka and Z. Was,
PHOTOS Monte Carlo: a precision tool for QED corrections in Z and W decays,
Eur. Phys. J. C **45** (2006) 97, arXiv: hep-ph/0506026.

[48] N. Davidson, T. Przedzinski, and Z. Was,
PHOTOS Interface in C++: Technical and physics documentation,
Comput. Phys. Commun. **199** (2016) 86, arXiv: 1011.0937 [hep-ph].

[49] D. J. Lange, *The EvtGen particle decay simulation package*,
Nucl. Instrum. Meth. A **462** (2001) 152.

[50] ATLAS Collaboration, *Measurement of the transverse momentum distribution of Drell–Yan lepton pairs in proton–proton collisions at* $\sqrt{s}$ = 13 *TeV with the ATLAS detector*,
Eur. Phys. J. C **80** (2020) 616, arXiv: 1912.02844 [hep-ex].

[51] M. Grazzini, S. Kallweit, S. Pozzorini, D. Rathlev, and M. Wiesemann,
W^+W^- *production at the LHC: fiducial cross sections and distributions in NNLO QCD*,
JHEP **08** (2016) 140.

[52] R. Frederix, E. Re, and P. Torrielli,
Single-top t-channel hadroproduction in the four-flavour scheme with POWHEG and aMC@NLO,
JHEP **09** (2012) 130, arXiv: 1207.5391 [hep-ph].

[53] ATLAS Collaboration, *Electron and photon performance measurements with the ATLAS detector using the 2015-2017 LHC proton-proton collision data*, JINST **14** (2019) P12006,
arXiv: 1908.00005 [hep-ex].

[54] ATLAS Collaboration, *Muon reconstruction and identification efficiency in ATLAS using the full Run 2 pp collision data set at* $\sqrt{s}$ = 13 *TeV*, Eur. Phys. J. C **81** (2021) 578,
arXiv: 2012.00578 [hep-ex].

[55] ATLAS Collaboration, *Muon reconstruction performance of the ATLAS detector in proton–proton collision data at* $\sqrt{s}$ =*13 TeV*, Eur. Phys. J. C **76** (2016) 292, arXiv: 1603.05598 [hep-ex].

[56] ATLAS Collaboration,
Topological cell clustering in the ATLAS calorimeters and its performance in LHC Run 1,
Eur. Phys. J. C **77** (2017) 490, arXiv: 1603.02934 [hep-ex].

[57] M. Cacciari, G. P. Salam, and G. Soyez, *The anti-*k_t *jet clustering algorithm*, JHEP **04** (2008) 063,
arXiv: 0802.1189 [hep-ph].

[58] M. Cacciari, G. P. Salam, and G. Soyez, *FastJet user manual*, Eur. Phys. J. C **72** (2012) 1896,
arXiv: 1111.6097 [hep-ph].

[59] ATLAS Collaboration, *Jet energy scale measurements and their systematic uncertainties in proton–proton collisions at* $\sqrt{s}$ = 13 *TeV with the ATLAS detector*, Phys. Rev. D **96** (2017) 072002,
arXiv: 1703.09665 [hep-ex].

[60] ATLAS Collaboration, *Performance of pile-up mitigation techniques for jets in pp collisions at* $\sqrt{s}$ = 8 *TeV using the ATLAS detector*, Eur. Phys. J. C **76** (2016) 581,
arXiv: 1510.03823 [hep-ex].

[61] ATLAS Collaboration, *ATLAS b-jet identification performance and efficiency measurement with $t\bar{t}$ events in pp collisions at $\sqrt{s}$ = 13 TeV*, Eur. Phys. J. C **79** (2019) 970, arXiv: 1907.05120 [hep-ex].

[62] ATLAS Collaboration, *E_T^{miss} performance in the ATLAS detector using 2015-2016 LHC p-p collisions*, tech. rep. ATLAS-CONF-2018-023, CERN, 2018, URL: https://cds.cern.ch/record/2625233.

[63] ATLAS Collaboration, *Performance of missing transverse momentum reconstruction with the ATLAS detector using proton-proton collisions at $\sqrt{s}$ = 13 TeV*, Eur. Phys. J. C **78** (2018) 903, arXiv: 1802.08168 [hep-ex].

[64] ATLAS Collaboration, *Performance of electron and photon triggers in ATLAS during LHC Run 2*, Eur. Phys. J. C **80** (2020) 47, arXiv: 1909.00761 [hep-ex].

[65] ATLAS Collaboration, *The ATLAS Inner Detector Trigger performance in pp collisions at 13 TeV during LHC Run 2*, (2021), arXiv: 2107.02485 [hep-ex].

[66] ATLAS Collaboration, *Performance of the ATLAS muon triggers in Run 2*, JINST **15** (2020) P09015, arXiv: 2004.13447 [physics.ins-det].

[67] ATLAS Collaboration, *Electron and photon performance measurements with the ATLAS detector using the 2015–2017 LHC proton-proton collision data*, JINST **14** (2019) P12006, arXiv: 1908.00005 [hep-ex].

[68] G. Cowan, K. Cranmer, E. Gross, and O. Vitells, *Asymptotic formulae for likelihood-based tests of new physics*, Eur. Phys. J. C **71** (2011) 1554, [Erratum: Eur.Phys.J.C 73, 2501 (2013)], arXiv: 1007.1727 [physics.data-an].

[69] ATLAS Collaboration, *Jet energy resolution in proton–proton collisions at $\sqrt{s}$ = 7 TeV recorded in 2010 with the ATLAS detector*, Eur. Phys. J. C **73** (2013) 2306, arXiv: 1210.6210 [hep-ex].

[70] ATLAS Collaboration, *Measurement of the Inelastic Proton–Proton Cross Section at $\sqrt{s}$ = 13 TeV with the ATLAS Detector at the LHC*, Phys. Rev. Lett. **117** (2016) 182002, arXiv: 1606.02625 [hep-ex].

[71] ATLAS Collaboration, *Muon reconstruction performance of the ATLAS detector in proton–proton collision data at $\sqrt{s}$ = 13 TeV*, Eur. Phys. J. C **76** (2016) 292, arXiv: 1603.05598 [hep-ex].

[72] ATLAS Collaboration, *ATLAS Computing Acknowledgements*, ATL-SOFT-PUB-2021-003, URL: https://cds.cern.ch/record/2776662.